Nanoparticle adhesion in proton exchange membrane fuel cell electrodes

Qianping He [a], David C. Joy [b,c], David J. Keffer [b,*]

[a] Department of Chemical and Biomolecular Engineering, University of Tennessee, Knoxville, TN 37996, USA
[b] Department of Materials Science and Engineering, University of Tennessee, Knoxville, TN 37996, USA
[c] Center for Nanophase Materials Science, Oak Ridge National Laboratory, Oak Ridge, TN 37830, USA

HIGHLIGHTS

- MD simulations investigate the binding energy and force of Pt nanoparticles on graphite.
- Adhesion of Pt nanoparticles to graphite is a function of particle shape.
- Adhesion of Pt nanoparticles to graphite is a function of particle size.
- Adhesion of Pt nanoparticles to graphite is enhanced by a Nafion film.
- The hydration of Nafion has a complicated effect on Pt nanoparticle adhesion.

GRAPHICAL ABSTRACT
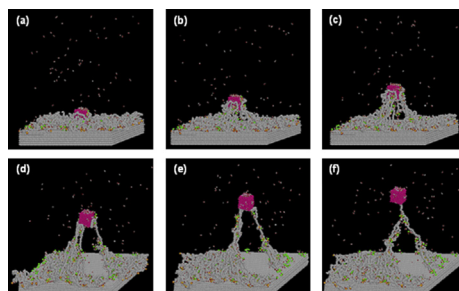
ARTICLE INFO

ABSTRACT

Carbon supported platinum (Pt/C) catalyst remains among the most preferable catalyst materials for Proton Exchange Membrane (PEM) fuel cells. However, platinum (Pt) particles suffer from poor durability and encounter electrochemical surface area (ESA) loss under operation with the accompany of Pt nanoparticle coarsening. Several proposed mechanisms have involved the Pt detachment from its carbonate support as an initial step for the deactivation of Pt nanoparticles. In this study, we investigated the detachment mechanism from the nano-adhesion point of view. Classic molecular dynamics simulations are performed on systems contain Pt nanoparticles of different sizes and shapes. A thin Nafion film (1 nm) at different hydration levels is also included in the system to study the environmental effect on nanoparticle adhesion. We found that the adhesion force strengthens as the Pt size goes up. Pt nanoparticles of tetrahedral shape exhibit relatively stronger connection with the carbon substrate due to its unique 'anchor-like' structure. Adhesion is enhanced with the introduction of a Nafion. The humidity level in the Nafion film has a rather complicated effect on the strength of nanoparticle adhesion. The binding energies and maximum adhesive forces are reported for all systems studied.

© 2013 Elsevier B.V. All rights reserved.

1. Introduction

Proton Exchange Membrane (PEM) fuel cells are the most popular type of fuel cells, due to their high energy conversion efficiency and power density, fast startup and low/zero emission level [1]. Yet, their further commercialization is limited at the current stage by technological bottlenecks. For example, the durability of fuel cells, especially the catalyst stability, remains one of the primary limitations for PEM fuel cells [2–6]. According to a recent review, the lifetime of transportation PEM fuel cells still need to be doubled to meet the DOE's target (5000 h) compared with lifetime value achieved in 2009 (2500 h) [7]. A molecular-level understanding of the mechanisms of the catalyst deactivation is needed to seek the next generation of fuel cell materials with improved performance and prolonged operating life.

* Corresponding author. Tel.: +1 865 974 5322; fax: +1 865 974 7076.
E-mail address: dkeffer@utk.edu (D.J. Keffer).

Carbon supported platinum catalyst (Pt/C) has remained among the most preferable catalyst materials for PEM fuel cells. It has very high kinetics for the hydrogen oxidation reaction (HOR) and one of the best electrode performances at low temperature and in the acidic environment inside PEM fuel cells [8]. However, previous studies have found that platinum (Pt) particles suffer from poor durability and will rapidly lose electrochemical surface area (ESA) under operation [9–14]. The process is usually accompanied with the behavior of Pt nanoparticle growth. Ferreira et al. proposed three fundamentally different mechanisms of Pt deactivation: (i) platinum dissolution and redeposition (the Ostwald ripening process), (ii) coalescence of platinum nanoparticles via platinum nanocrystallite migration on the carbon support and (iii) platinum particle agglomeration triggered by detachment of Pt particles from the carbon support (caused by carbon corrosion) [9]. Recently, Mayrhofer's group proposed a new corrosion mechanism for Pt catalyst, demonstrating that whole Pt particles can detach from the support and dissolve into the electrolyte without redeposition [15]. Huang's group also reported the observation of detachment of small Pt clusters from the carbon support in their MD simulations [16]. Besides, TEM images of catalyst materials before and after testing indicate that many platinum particles are not sufficiently anchored to the carbon support and move into the ionomers portion of the catalyst layer before such testing as potential cycling [17]. Furthermore, Groves et al. has attributed the Pt catalyst detachment and agglomeration to the weak interaction between the Pt and carbon support [18]. And this mechanism is also mentioned in several review papers regarding the durability enhancement of carbon supported platinum catalyst [19,20]. Experimental evidence also substantiates the link between binding energy and catalyst durability. For example, doping fullerenes with nitrogen increases the binding energy and also shows an increase in dispersion of platinum, a resistance to agglomeration of nanoparticles, and a less significant deterioration of activity when compared with pure carbon cases [21–26]. It is possible that a combination of mechanisms contribute to the observed Pt agglomeration and ESA loss. This fact has motivated many studies into agglomeration mechanism of Pt catalyst in PEM fuel cells [2,8,9,11,15,27–29]. For example, Bi et al. proposed a physical based Pt/C catalyst model with a simplified bi-modal particle size distribution and they were able to clearly demonstrate the catalyst coarsening with Pt nanoparticle growth [2]. Diloyan et al. investigated the effect of mechanical vibration on Pt particle agglomeration [8]. More et al. believe that a combination of Pt particle coalescence and Pt solution/re-precipitation within the solid ionomer is the mechanism predominantly responsible for Pt degradation [30]. Groves et al. investigate the binding energy between one Pt atom and five different graphene surfaces (one pure and four singly doped with beryllium, boron, nitrogen, and oxygen) to explore the most stable Pt-surface bond, and they believe that by finding the highest binding energy surface, the durability of a platinum catalyst can be greatly improved [18].

Many of the mechanisms discussed above originate in detachment of the Pt nanoparticle from the substrate surface, which could possibly arise from a weak binding energy between the catalyst and the carbon support. When the interaction between Pt and its substrate is not strong enough, nanoparticle detachment could easily happen under certain conditions. For example, the mechanical vibration during the automobile transportation when fuel cells are used as an alternative energy source in vehicular applications could cause shearing stresses between the bipolar plate (BP), gas diffusion layer (GDL) and membrane electrode assembly (MEA), which may lead to the deformation of MEA including the catalyst layer. The deformation of materials surrounding the Pt nanoparticles on the carbon substrate may cause the Pt nanoparticle to detach from the carbon substrate, especially in cases when Pt nanoparticles are not sufficiently anchored to the carbon support. Besides, the formation of perforations, cracks, tears or pinholes on fuel cell membrane and catalyst layer as a result of degradation could also cause external force such as detachment force on Pt nanoparticles. Therefore, investigating the nanoparticle adhesion between Pt and its carbon support could help us characterize the strength of the nanoparticle interaction with the substrate, and thus allow us to estimate how easily Pt could be detached from the carbonate support, providing both a better fundamental understanding of the mechanisms in ESA loss as well as addressing practical issues such as whether the common vibrations in automobile transportation are sufficient to induce Pt detachment.

In this work, a set of molecular dynamics (MD) simulations calculating the nanoparticle adhesion between Pt and its carbon support is conducted to study the effect of nano-adhesion on the platinum nanoparticle detachment mechanism. Specifically, the effect on adhesion of nanoparticle size, nanoparticle shape, presence of polymer electrolyte binding film, and extent of hydration are investigated. The details of the simulations, results and conclusion are presented in the following sections.

2. Simulation methodology

In the work described here, classical molecular dynamics (MD) simulations in the canonical (NVT) ensemble are performed using an in-house code written in Fortran 90 and parallelized using MPI to determine the adhesion energy and force of platinum nanoparticles on a carbon surface, intended to represent the part of the catalyst layer of a PEM fuel cell. The Pt nanoparticles are equilibrated on either a clean carbon surface or on a surface upon which a hydrated Nafion film is present. Once equilibrated the nanoparticles are pulled from the surface at a constant velocity via an externally applied force. From these simulations, the binding energy and force are measured. The molecular-level mechanisms responsible for variations in adhesion are also revealed.

Catalytic activity of Pt nanoparticles is strongly dependent on the particle size, shape and morphology. And with the advance of modern synthetic technology, Pt nanoparticles can be synthesized with various shapes (cubes, tetrahedrons, octahedrons, decahedrons, icosahedrons) bounded by different number of facets and with different defects [21,31,32]. All of these shapes were found successfully synthesized in a Nafion recast film with high yields [33–35]. In this work, four nanoparticle shapes—cubic, tetrahedral, truncated octahedral and octahedral nanoparticles—were simulated. For each shape, three nominal sizes—2 nm, 4 nm and 6 nm—were simulated. The number of atoms in the nanoparticle ranged from 56 (2 nm tetrahedron) to 14,896 (6 nm cube). As to the choice of nanoparticle size, we followed Ferreira et al. [9], who performed a size distribution analysis of 200 Pt nanoparticles in the pristine Pt/C sample and powders scraped from the cycled membrane electrode assembly (MEA) cathode surface. They found a mean particle diameter of 2.8 nm for pristine Pt/C and 5.9 nm for the cycled sample.

The nanoparticles were obtained from the bulk Pt crystal with an fcc structure, with corresponding lattice parameters ($a = b = c = 0.392420$ nm and $\alpha = \beta = \gamma = 90°$) and space group of Fm-3m [36]. The various shaped nanoparticles were obtained by making cuts in the bulk crystal along the appropriate planes. The cutting planes were different depending on the shape and were always parallel to the face that had to be exposed in each case. For example for the cubic shape, three cuts were made with planes parallel to the {1 0 0}, {0 1 0} and {0 0 1} faces. Thus a cubic particle enclosed by six 1 0 0 faces was built. The Pt models used in this work are defect free. While it is known that there are slight changes
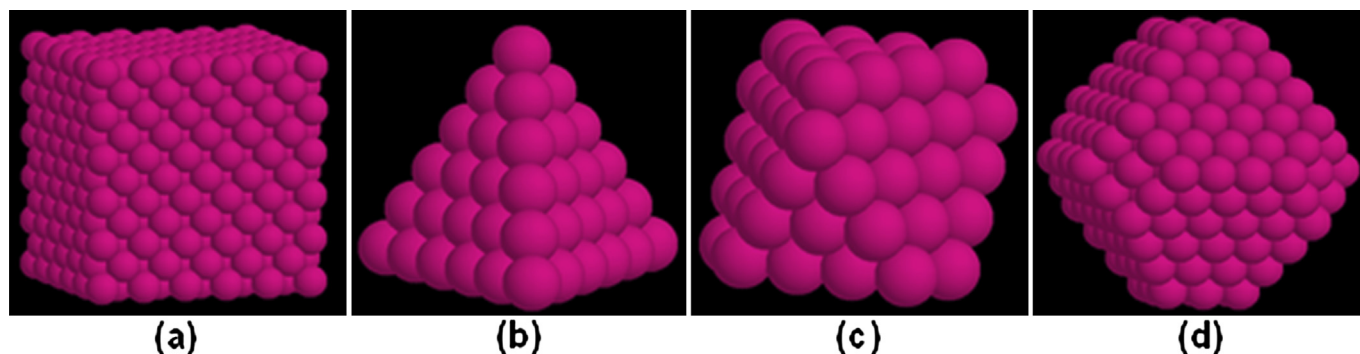
Fig. 1. Molecular models for the platinum nano-particle. (a) Tetrahedron (b) cube (c) octahedron (d) truncated octahedron. Color legend: pink is platinum. (For interpretation of the references to color in this figure legend, the reader is referred to the web version of this article.)

in lattice parameter as the size of the Pt nanoparticle decreases, that effect was not incorporated here [37]. Snapshots of the isolated Pt nanoparticles used in the simulation are shown in Fig. 1. It should be mentioned that in this work Pt nanoparticles remain isolated since this work focuses on the interaction between Pt and its carbon support rather than the interaction among Pt nanoparticles. The detachment of Pt nanoparticles is considered the first step in agglomeration of Pt nanoparticles. However, agglomeration is not modeled in the simulations.

Although carbon black (amorphous carbon) such as Vulcan XC-72 from E-TEK has been commonly used in industry as the carbon support for PEM fuel cells at the current stage [38], the carbon electrode is modeled as graphite here. The choice is justified by the following considerations. First, compared with the amorphous carbon, graphite possesses more π sites (sp^2-hybridized carbon), which plays the role of anchoring centers for Pt [39] and thus will result in a strengthened metal−support interaction and the resistance of Pt to sintering [40]. Second, with the development of catalyst structure, graphitized carbon support of enhanced catalyst activity (which was formerly the reason that graphitic carbon was not chosen as the fuel cell carbon support) has been developed [41−44]. Third, increasing attention is paid to the application of graphitic carbon (e.g. graphite nanofibers) as the catalyst support [45−47]. Last but not the least, at the nanoscale, there is similarity in the structure of graphite and graphite nanofibers and the most reliable atomic data is available for the graphite model. The model is thus built by first obtaining a unit cell structure with corresponding unit cell parameters (a = 0.2461 nm, c = 0.6708 nm, Z = 4) and space group (P6$_3$/mmc) [48]. The unit cell is extended in x, y, z directions until the targeted size is achieved. The final structure used in our simulations contains seven layers to meet our cut-off distance (2.1 nm). The use of the seven-layer graphite model is further justified by a calculation of the contribution of each

graphite layer to the potential energy result. According to the calculation, it is found that at equilibrium separation distance (~0.3 nm), the first and second layer of the graphite contribute more than 99% to the results. And with the separation distance increasing, the role of the latter layers of graphite become important, for example, at 1.3 nm separation distance, the first three layers contribute 70%, 20% and 7% to the results respectively; and at largest separation distance, an almost even contribution of each layer to the result is obtained. However, since the potential energy approaches zero at large separation distance, the contribution distribution is less important. Thus, seven layers are believed to be sufficient for the graphite model in the simulation. The lateral dimensions of the graphite slab are 17.3 nm and 14.7 nm. A snapshot of the graphite model used in our simulation is shown in Fig. 2. In this work, we did not include any oxidation or defects on the graphite surface, thus only the perfect graphite model is considered. The effect of oxidation of the surface is planned for a subsequent publication. For more details about all the molecular structures involved in this work, please refer to our online archived site [49].

Recast polymer electrolyte is frequently included in the catalyst layer in order to provide a path for proton transport from the catalyst particle to the proton exchange membrane. In this work, Nafion, as the most common perfluorosulfonic acid PEM material used industrially, is selected as the recast polymer electrolyte. The model of Nafion used in this work has been previously used to study the bulk hydrated membrane [50,51]. The model consists of 15 monomers with an equivalent weight (EW; the molecular weight of the repeat unit) of 1144. See Fig. 3. The film thickness is chosen to be nominally 1 nm to avoid the Pt particle being totally buried in the film (our smallest Pt particle measures 2 nm). Experimentally, there is an optimal recast Nafion content in the catalyst layer [52], because too little Nafion fails to provide a path
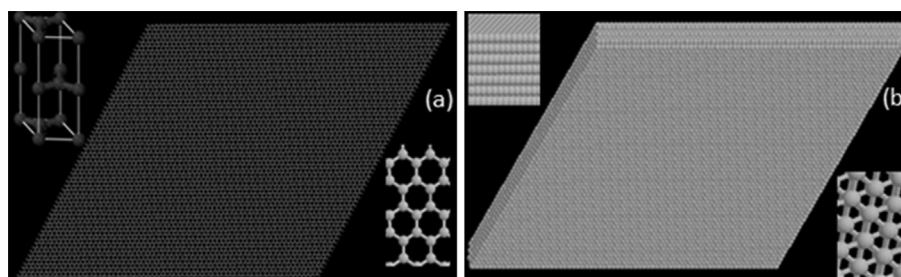

Fig. 2. Graphite model. (a) Single plane of graphite model with the graphite unit cell in the top left corner and a top view close-up of the graphite layer in the bottom right corner (b) seven-plane graphite model used in our simulation with a side view close-up in the top left corner and top view close-up in the bottom right corner. Color legend: gray is carbon.
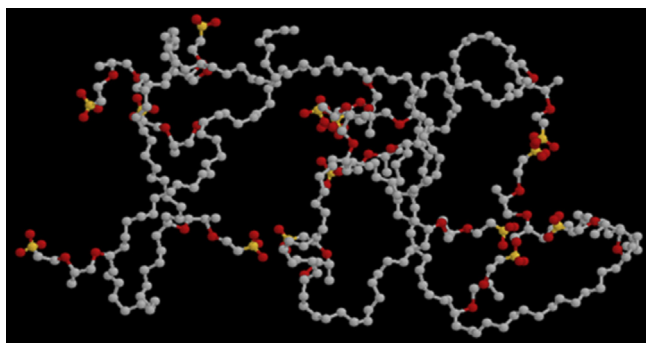
Fig. 3. Nafion model. A single chain is shown. Color legend: gray is CF_x, orange is sulfur, red is oxygen. (For interpretation of the references to color in this figure legend, the reader is referred to the web version of this article.)

for proton transport and too much buries the catalyst particles, presenting a mass-transfer barrier for the hydrogen fuel (at the anode). This thin film is an attempt to represent the desirable triple phase boundary of Nafion/Pt/gas and the choice of 1 nm thickness is believed to be reasonable, as it represents a film that will not completely cover the nanoparticle but that provides a continuous path along the graphite surface. The system is analyzed at the nominal hydration levels of $\lambda = 3, 6, 9, 15$ H_2O/HSO_3. These hydration levels span the range from minimally hydrated to well hydrated [50]. The number of each component in the simulated system of different hydration levels and different Pt sizes is listed in Table 1.

The potentials for Nafion, water and the hydronium ions used in this work is identical to that of our previous work [50]. The Nafion model is fully atomistic except for CF_3, CF_2, and CF. These CF groups are treated as united atom to reduce computational costs [53–56]. The atoms of Nafion, water and hydronium ions are charged, which allows us to take into account the forces among ions. We have included bond stretching, bending, torsion, intramolecular and intermolecular nonbonded interactions via the Lennard-Jones (LJ) potential and Columbic interactions. The potential parameters of the Nafion model have been reported previously [50,57]. A TIP3P model with a flexible OH bond is used for the water model [58,59]. The hydronium ion is similar to that of Urata et al., we use the same partial charges for the oxygen and hydrogen atoms [60]. The bond distance, bond angles and force constants of hydronium ion are the same as in the TIP3P model [59]. Structural diffusion of protons is not allowed in our simulation given this potential; however this is not a limitation for the measurement of adhesion energies and forces.

The internal structures of the graphite layers as well as that of the Pt nanoparticle are rigid. We are aware of the phenomena of deformed nanoparticles with a neck when detaching from the adhesive substrates [61]. In those simulations, the classical Johnson, Kendall, and Roberts (JKR) [62] and the Derjaguin, Muller, and Toporov (DMT) [63] theories are used to describe the adhesive contact between the substrate and nano-particles. However, both JKR and DMT theories are developed for the adhesion of elastic

spheres on flat surfaces and their models fail to describe kinetic effect [64]. Moreover, according to Carrillo et al., the nanoparticle shape-changing process during detachment is accompanied by rupture of adhesion bonds formed between the nanoparticle and the substrate [61]. In other words, the interaction between the nanoparticle and substrate should be large enough to form adhesion bonds so that the nanoparticle shape has to be changed to resist the detachment process. However, the binding energy between Pt and carbon surfaces calculated by the density functional theory has shown that no formal bond is formed between the platinum atom and the pristine carbon surface [18]. Based on the above factors, nanoparticle shape transformation [61] during detachment process is not considered in our simulations.

In the adhesion analyses, the LJ interaction potential are widely accepted and used in modeling adhesive contacts [65–67]. The interaction of the carbon of graphite and platinum of the nanoparticle with other atoms in the system are represented by LJ potentials ($\varepsilon_{Pt}/k = 2336.0$ K, $\sigma_{Pt} = 0.241$ nm, $\varepsilon_{graphite}/k = 28.0$ K, $\sigma_{graphite} = 0.34$ nm) [68–70]. It is worth pointing out here that although the LJ parameters for Pt were originally developed for the simulation of adsorption of Pt on graphite walls, our previous work has proven that it's also suitable to describe the interaction between Pt and organic molecules, such as Nafion, water and hydronium ion based on the fact that our simulations results match quite well with the results obtained from atomic level experiments (scanning tunneling microscope; core-level spectroscopy, i.e., XPS, XES, XAS; He atom scattering spectrum) as well as quantum mechanical calculations (DFT) [71]. The Lorentz-Berthelot mixing rules are invoked for all interspecies interactions, in order to maintain uniformity in the interaction potential and to remain consistent with the Nafion potential, which used them in its parameterization [53–56]. For the calculation of the electrostatic interactions, the spherically truncated, charge neutralized method of Wolf et al. is applied [72]. The Nosé–Hoover thermostat is employed to maintain the system at a constant temperature of 298 K [73,74]. The two time scale r-RESPA method is incorporated to integrate the equations of motion with 1 fs for the large time step size and 0.1 fs for the intramolecular degrees of freedom [75].

Considering the parallelogram shape of graphite surface, a non-cubic simulation box is used in this simulation. The simulation box has an x-length of 14.7 nm, y-length of 17.3 nm and z-length of 40.0 nm. The z-length was chosen to be sufficiently large to avoid non-physical contributions from periodic images of the system in the z-dimension. The angle from x-axis to y-axis is equal to 60°. The Pt nanoparticle supported over the graphite surface was fixed at the bottom of our simulation box with the Pt nanoparticle sitting in the center of graphite surface at the equilibrium distance of the bare system. The equilibrium distance between Pt nanoparticle and graphite is obtained by plotting the LJ potential of Pt and graphite versus different separation distances ranging from 0 to 20 nm.

The initial configuration of Nafion, water molecules and hydronium ions were randomly placed around the Pt in the system. In order to avoid a physical overlap, equilibration involved first a brief period (20 ps) of growing the atoms of Nafion, water and hydronium ion, by gradually increasing the LJ collision diameter. The

Table 1
The number of water, hydronium ion and Nafion chains in each system.

Pt size	2 nm				4 nm				6 nm			
λ (H_2O/SO_3H)	3	6	9	15	3	6	9	15	3	6	9	15
Number of Nafion	14	13	12	10	14	13	12	10	12	11	10	9
Number of H_2O	420	975	1440	2100	420	975	1440	2100	360	825	2100	1890
Number of H_3O^+	210	195	180	150	210	195	180	150	180	165	150	135

"growing" of atoms is a standard technique for molecular simulation of dense but non-crystalline systems, which allows one to recreate a reasonable molecular-level initial estimate of the structure that does not contain any overlap of atoms that could potentially result in unphysically large forces. This structure is thoroughly equilibrated before any data production begins.

Fig. 4 is a snapshot of an equilibrated system containing a 2 nm cubic Pt nanoparticle at the hydration level of $\lambda = 3$. The equilibrated system possesses displays several characteristic features. The Nafion molecules form a film on the surface. Some of Nafion forms a film around the nanoparticle. Water molecules and hydronium ions cluster around the sulfonic acid groups. Some small fraction of water molecules enter the vapor phase.

After the system is equilibrated, the Pt nanoparticle is pulled from the graphite surface along the z-axis at a constant speed of 0.01 nm fs^{-1}. The choice of constant speed is based on the two facts. First, the maximum adhesion force depends weakly on the pulling velocity while the nanoscale intermittent behavior of species during the detachment process depends strongly on the pulling velocity [76]. Therefore, it is believed that the focus of this paper, i.e., the effect of nanoparticle size, shape and the introduction of hydrated polymer on the nanoparticle adhesion will not be strongly affected by the choice of pulling velocity. Second, many experiments involving the measurement of nano-adhesion use constant pulling velocity [77,78]. To be compatible with the experiments and to keep our systems comparable, constant pulling speed is applied throughout the simulation.

The potential energy and force for the nanoparticle are computed at each separation between nanoparticle and surface. The reported potential energy of the nanoparticle is the sum of all interactions between Pt atoms and all other atoms in the graphite surface and film.

$$U = 4 \sum_{i=1}^{N_{Pt}} \sum_{j=1}^{N_{SUR}+N_{FILM}} \varepsilon_{ij} \left[(\sigma_{ij}/r_{ij})^{12} - (\sigma_{ij}/r_{ij})^{6} \right] \quad (1)$$

(See nomenclature for definition of symbols.) The reported force on the nanoparticle is the z-component (normal to the graphite surface) of the force between Pt atoms and all other atoms in the graphite surface and film.

$$F_z \equiv -\partial U / \partial z = 24 \sum_{i=1}^{N_{Pt}} \sum_{j=1}^{N_{SUR}+N_{FILM}} \varepsilon_{ij} \left[2(\sigma_{ij}/r_{ij})^{12} - (\sigma_{ij}/r_{ij})^{6} \right] z_{ij}/r_{ij}^{2} \quad (2)$$

We note that because the Pt atoms are not charged, there is no explicit Coulombic term in Eq. (1) or Eq. (2). However, there are Coulombic interactions between the Nafion, water, and hydronium ions, which impact their distribution and thus indirectly effect the energy and forces on the nanoparticle. A list of the major assumptions made in this simulation is summarized in Table 2.

Table 2
The major assumptions made in the simulation.

Assumptions:
1. The carbon electrode is modeled as pristine graphite.
2. The graphite model is defect free and contains 7 layers.
3. The Pt nanoparticle is defect free and oxidation free.
4. Slight changes in the Pt lattice parameter due to size are ignored.
5. The internal structures of Pt and graphite are rigid.
6. There is only one platinum nanoparticle in the simulation box.
7. The CF groups in the Nafion molecules are treated as united atoms.
8. Structural diffusion of proton is not allowed.

3. Results and discussion

We begin the results and discussion section by presenting results from the bare system, in which there is no Nafion or water present. The results of the bare system do not require MD simulations, simply energy and force evaluations as a function of separation between the Pt nanoparticle and graphite surface, which is different from any other systems that contain water and ionomers. The inclusion of the dry systems is intended to provide a baseline by which the impact of water and polymer film can be measured.

3.1. Bare systems

In Fig. 5(a) and (b), the potential energy and normal force between the Pt and graphite (bare system) are plotted as a function of separation between the nanoparticle and surface for several nanoparticle sizes of cubic shape. Here the separation distance is defined as the distance between the center of carbon atoms forming the top layer of graphite and the center of Pt atoms forming the bottom layer of nanoparticle. The 'bare system' curve represents the cumulative LJ interaction between the nanoparticle and the surface. As shown in figure, when Pt and graphite are far apart, the interaction energy and force are zero. As the distance of separation decreases, there are dispersive interactions that give rise to a potential energy well and a corresponding attractive (negative) force. There is a minimum in the energy well at a distance where the nanoparticle is resting on the surface. The minimum in this energy well corresponds to the binding energy. At separations smaller than this equilibrium distance, the force is positive and the energy quickly increases due to repulsion between the C and Pt atoms.

For a cubic particle of size varying from 2 to 6 nm, the well is deeper for larger particles, simply because there are more Pt atoms in larger particles contributing to the attractive interaction. In Fig. 5(a) and (b), the net energy and force are plotted on a per particle basis rather than a per atom basis. On a per atom basis, the difference in the force and energy curves as a function of nanoparticle size is reduced, but the curves do not perfectly overlap, because the distribution of distance between Pt and C atoms is
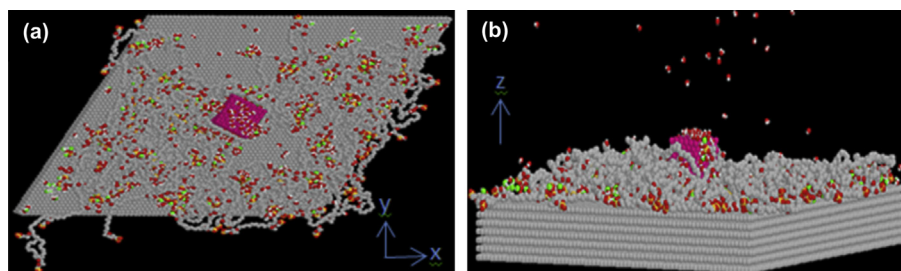

Fig. 4. Snapshot of an equilibrated system contains a 2 nm cubic Pt nanoparticle at the hydration level of $\lambda = 3$. (a) Top view (b) side view.
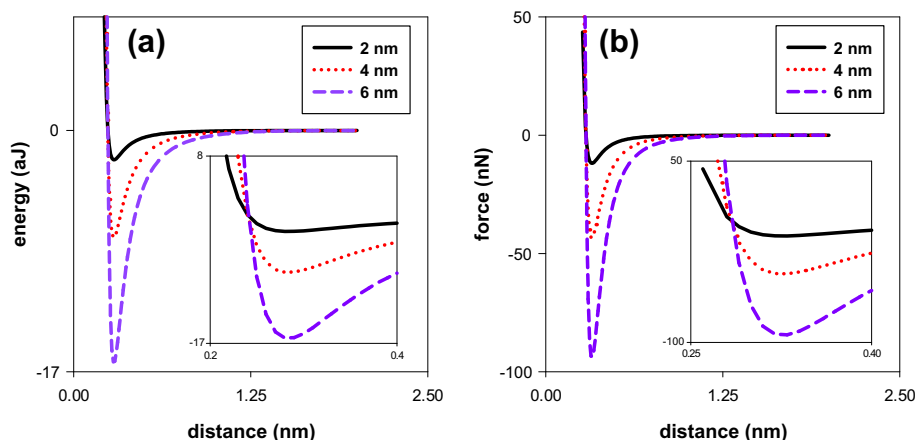
Fig. 5. Potential and force curves for bare systems contain a cubic Pt of different sizes. (a) Potential curve (b) force curve.

different for nanoparticles of different size. It should be pointed out that the binding energy per atom increases in magnitude as the size of the particle decreases, because in small nanoparticles a greater fraction of the Pt atoms are located closer to the minimum in the Lennard-Jones pairwise interaction potential. For example, these three sizes of nanoparticle cubes, the binding energy per Pt atom is −0.0031, −0.00163, −0.00109 aJ/Pt atom respectively with increasing size. It is also observed that the position of the equilibrium distance (where the force is zero) is relatively insensitive to nanoparticle size, since this position is largely dictated by repulsion between the top layer of graphite and the bottom layer of Pt.

From a quantitative point of view, the binding energies for these cubic nanoparticles on clean graphite range from −16.3 to −2.1 aJ for the 6 nm to the 2 nm nanoparticles respectively. This range of binding energies can be alternatively expressed as −9815 to −1242 kJ mol^{-1} of nanoparticles or as −0.66 to −1.9 kJ mol^{-1} of Pt atom. Similarly, the adhesion forces for these nanoparticles on clean graphite range from −93.8 to −11.9 nN (per particle) for the 6 nm to the 2 nm nanoparticle respectively.

In Fig. 6(a) and (b), the potential energy and normal force between the Pt and graphite (bare system) are plotted as a function of separation between the nanoparticle and surface for several nanoparticle shapes with nominal size of 2 nm. The number of Pt atoms in each nanoparticle varies and is reported in Table 3. The cube has the most Pt atoms with 666 and the tetrahedron, made by cutting the 2 nm cube into a tetrahedral shape has only 56 atoms. The depth of the energy well corresponds to the number of Pt

atoms in the nanoparticle except for the pair of "tetrahedron and octahedron". The tetrahedron has a slightly deeper energy well compared with the octahedron although it has the least number of atoms. This might be attributed to the fact that more atoms are located closer to the minimum in the Lennard-Jones pairwise interaction potential in tetrahedral Pt compared with the octahedron. However, plots of the energy on per Pt atom basis show a much smaller difference between particles of varying shape but do not fall on a unique master curve because the distribution of distances of Pt atoms from the graphite surface is a function of the nanoparticle shape. The binding energy on a per Pt atom basis are reported in Table 4. We observe that the binding energy on a per particle basis does not have an obvious relationship with the total number of atoms in each shape. Instead, it is related with the ratio of number of atom at the bottom portion to the upper portion. When a larger portion of atoms are located in the bottom layer, it has a stronger binding energy. Thus the tetrahedron, (the majority of whose atoms are located closer to the bottom) has the highest binding energy.

3.2. Wet systems

In this section, we discuss the results of Pt nanoparticle adhesion on wet systems. These systems contain a film of Nafion on the graphite surface at various hydration levels. This recast Nafion serves as a path for proton transport from the catalyst nanoparticle to the proton exchange membrane. It also acts as a binder for the
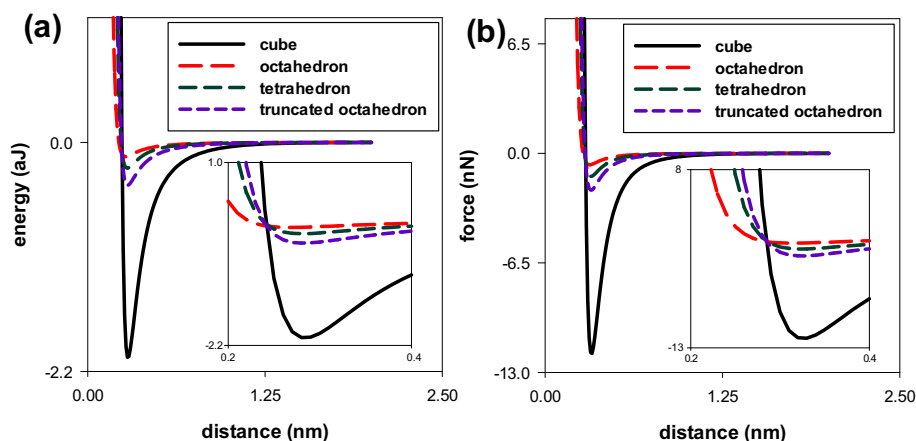

Fig. 6. Potential and force curves for bare systems contain a 2 nm Pt of different shapes. (a) Potential curve (b) force curve.

Table 3
The number of atoms in each Pt nanoparticle.

	2 nm	4 nm	6 nm
Cube	666	4631	14896
Tetrahedron	56	364	1540
Truncated octahedron	314	2735	8000
Octahedron	80	660	2240

Table 5
Average number of water molecules retained in the film for the 2 nm cubic Pt systems of different hydration levels.

Hydration level	$\lambda = 3$	$\lambda = 6$	$\lambda = 9$	$\lambda = 15$
Average number of H_2O and H_3O^+ retained in the film	557	843	1167	1757
Actual film λ	2.65	4.32	6.48	11.71

nanoparticles. Sufficient Nafion is placed to form a uniform film of 1 nm thickness. However, none of the simulation snapshots reveal a uniform film, since the hydrated Nafion aggregates into clusters and does not remain distributed on the hydrophobic clean graphite surface. Furthermore, nominal water contents of $\lambda = 3$, 6, 9 and 15 H_2O/HSO^3 are investigated. Previous simulations of hydrated Nafion at the membrane/vapor interface or at the membrane/catalyst/vapor and membrane/graphite/vapor three-phase interfaces show that virtually all of the water is retained in the membrane for $\lambda = 3$ through 21 H_2O/HSO^3, with roughly only one molecule or less entering the vapor phase at any instant in time [79,80]. In this work, we use the nominal water contents are provided, but it is observed that much of the water leaves the film and enters the vapor phase. This is consistent with experimental observations that the ability for Nafion to retain moisture decreases as the membrane thickness decreases [81]. It should be pointed out here that the evaporation of water molecules into the vapor phase does not affect the relationship between the λ value and hydration level, i.e., it is still true that a higher λ value represents a higher hydration level. We have verified this by calculating the average number of water molecules retained in the Nafion film for the 2 nm cubic Pt systems of different λ values. Results are presented in Table 5.

Calculation of the binding energy and adhesion forces from the wet simulations involves two components. The first is the energy and force between the rigid graphite surface and the rigid Pt nanoparticle. These energies and forces vary smoothly with separation as shown in Figs. 5 and 6. (This is the only contribution present in the dry systems.) The wet systems have a second contribution to the binding energy and adhesion forces, which are due to the interaction between the Pt atoms and the dynamic molecules in the system, including the Nafion, water molecules and hydronium ions. If these particles remained as a film, their contribution to the binding energy and adhesion force would remain unambiguous. Since some of the water enter the vapor phase, the reported binding energy will of necessity include some energy from water adhered to the Pt surface. It is worth pointing out here that compared to the dry system, the wet system exposed interesting phenomena such as polymer bridging etc., which makes the calculation of potential and force more complicated and difficult to estimate by simple back-of-the-envelope calculations.

3.2.1. Effect of Nafion at different humidity levels on Pt adhesion

Fig. 7 shows the potential energy versus separation distance curve for systems containing a cubic Pt particle of 2 nm with varying water content. In Fig. 7, it is clear that when Nafion and

Table 4
The binding energy for the 2 nm Pt nanoparticle.

2 nm Pt shape	Binding energy per Pt atom basis	Binding energy per Pt particle basis
Cube	−0.0031 aJ	−2.0633 aJ
Tetrahedron	−0.0044 aJ	−0.2467 aJ
Truncated octahedron	−0.0013 aJ	−0.4115 aJ
Octahedron	−0.0017 aJ	−0.1369 aJ

water are introduced to the system, the binding energy becomes stronger. Another immediately apparent feature of Fig. 7 is that the curves now contain fluctuations. On the smallest time scale (on the order of femtoseconds), these fluctuations are due to the dynamics of the mobile components (Nafion, H_2O and H_3O^+). At larger timescales (on the order of tens of picoseconds) these fluctuations are due to dynamics of relaxation processes of polymers in the system. Thus we observe non-monotonic trends in the binding energy as a function of separation. The molecular-level origin of this behavior will be discussed shortly.

In Fig. 8(a)–(f), a series of snapshots describing the detachment of the 2 nm cubic Pt nanoparticle from the wet surface ($\lambda = 3$) exposes the nature of this polymer relaxation. The nanoparticle is removed at a relatively high constant velocity. In this process, the polymer is both being stretched by the movement of the nanoparticle and is also undergoing internal relaxation both on the surface of the graphite and the surface of the nanoparticle. As the separation increases, the polymer is further stretched until, in the case of Fig. 8, it releases the nanoparticle and snaps back to the graphite surface.

In Fig. 9, the force curves for the 2 nm cubic Pt systems are presented at different hydration levels. The degree of fluctuation in the forces is much greater than that in the binding energy, and is so large that it obscures the interpretation of the data. The origin of these fluctuations, large when compared to experiment, is due to the very high temporal resolution (sampling frequency) of the simulations, which is 1 ps. Because of this extraordinarily high temporal resolution, the curve captures fluctuations due to the short-time scale dynamics of the polymer film. It also provides an abundance of data, greater than 10^5 data points for any given simulation. Thus some filtering of the data is necessary in order to observe the dependence of the force on properties such as degree of hydration.

A filtered result of Fig. 9 is shown in Fig. 10. Several filtering procedures were explored. A method is required preserves key features of the curves, such as the depth of the attractive well, but at the same time is capable of averaging out the temporal fluctuations. The filter used in this work is a combination of piecewise polynomial fitting and local averaging. The piecewise polynomial fitting is used at short lengths scales, less than 1 nm, to maintain the correct shape of the attractive well. Beyond 1 nm, local averaging is employed, which reduces the noise in a given spatial region, but also is capable of retaining distinct features due to observed molecular events. The local averaging was performed over a region of 1 nm and iteratively applied.

One can now study the binding energies of Fig. 7 and the filtered adhesion forces of Fig. 10 to understand the role of Nafion and water on nanoparticle adhesion. Compared to the bare system, Nafion at all water contents acts as a binding agent, increasing the magnitude of the binding energy and the adhesion force. The binding energy is increased by a factor of 4.31, 5.40, 4.63 and 4.61 for the $\lambda = 3$, 6, 9 and 15 respectively. The adhesion forces is increased by a factor of 1.40, 1.33, 1.26 and 1.32 for the $\lambda = 3$, 6, 9 and 15 respectively. However, it should again be pointed out here that strengthening the metal−support interaction by introducing a thicker film is not without limits because an excess of Nafion film in the catalyst layer
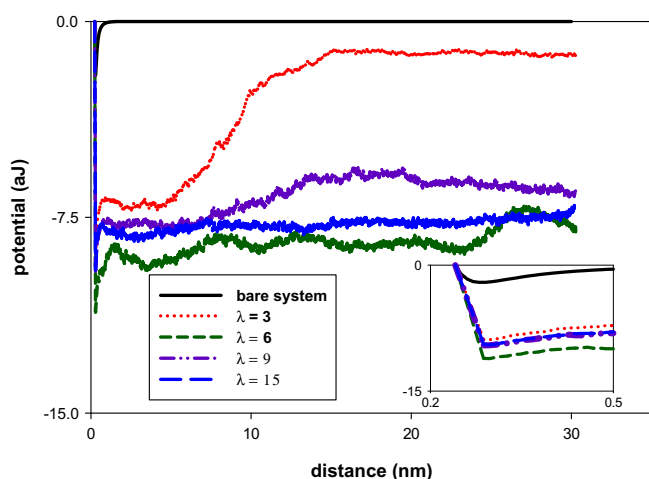
Fig. 7. Potential curves for systems contain a 2 nm cubic Pt and different hydration levels.

Fig. 9. Force curves for systems contain a 2 nm cubic Pt and different hydration levels.

will become a barrier for the reactant gas to access the reaction site and resulting in a malfunctioning fuel cell. It is worth noting that at large separations, the energy does not return to zero because the Pt nanoparticle has dragged water (and in some cases Nafion) from the surface with it. The forces do return to zero at large distances because the distribution of the water around the Pt nanoparticle is uniform and does not exert a net force in the normal direction to the graphite plane (or any other direction for that matter).

Even at short distances, the dependence of the binding energy and adhesion force between the nanoparticle and the surface as a function of water content is nonlinear. As we can observe in the inset of Fig. 10, the adhesion force decreases in magnitude from $\lambda = 3$, 6, and 9. In other words, in this range of water contents, the strength of adhesion weakens with increasing hydration. However, for the $\lambda = 15$ system, the maximum adhesion was slightly strengthened while it still does not exceed the maximum adhesion in $\lambda = 3$ system.
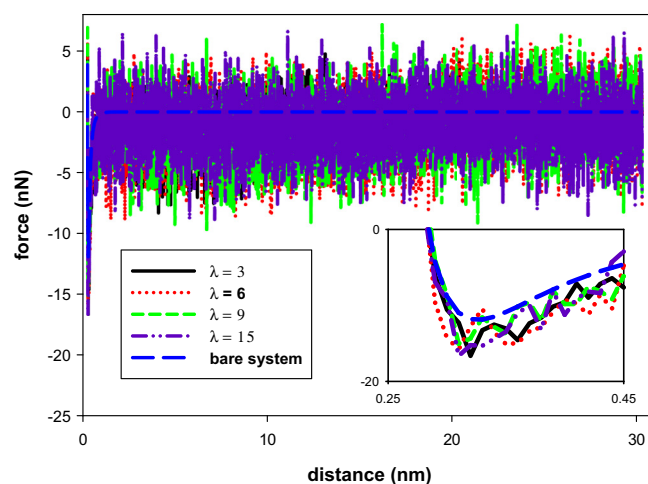
In an attempt to better understand the role that water plays in nanoparticle adhesion, it is important to separate out physical trends from statistical variation. In this work, only a single detachment event was performed for each combination of particle size, shape and water content. Therefore, our sampling is limited to a single event. As shown in Fig. 11, the distribution of Nafion, water and hydronium ion around the Pt and graphite surface right varies not only as a function of water content, but would also vary from one independent realization of the detachment event to another. Thus we report real, observed simulation results, which we believe to be typical and characteristic of each system. However, we also acknowledge that there is statistical variation that has not been quantified by this work. For example in some cases, the stretching of polymers as the Pt nanoparticle is removed from the graphite surface is observed (as shown in Fig. 8) and in other cases, it is not observed. However, all phenomena reported here are observed in a sufficient number of different cases (a total number of 20
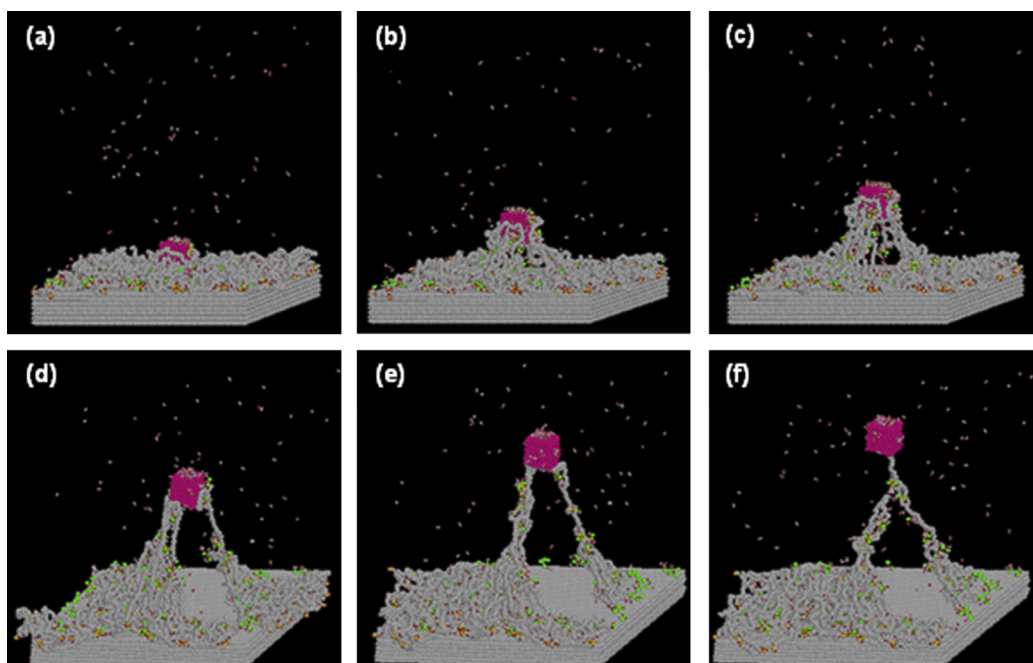

Fig. 8. Snapshots illustrating the process of Pt detachment from the graphite surface for a system includes a 2 nm cubic Pt at the hydration level of $\lambda = 3$.
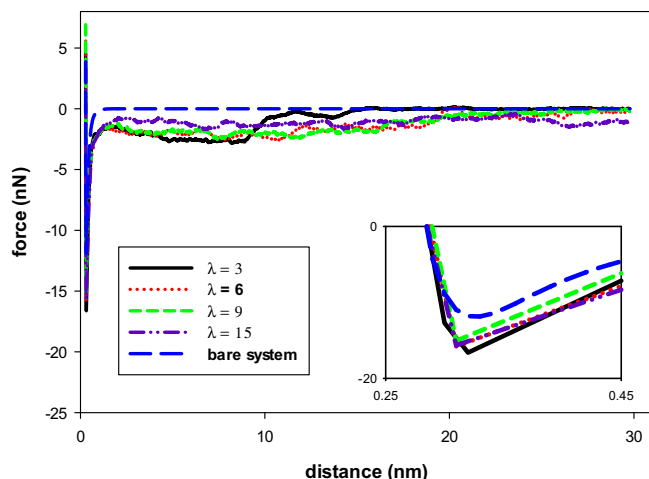
Fig. 10. Filtered force curves for systems contain a 2 nm cubic Pt and different hydration levels.

simulations were performed) for one to reliably accept that we did not observe a rare one-in-a-million event. For example, the phenomenon of polymer bridging is observed in many of these simulations.

With these cautionary disclaimers behind us, in Fig. 11, we observe that as Nafion aggregated into non-uniform clusters on the graphite surface, part of the cluster maintained contact with the Pt nanoparticle at $\lambda = 3$, 6, and 9. However, at $\lambda = 15$ there is preferential adsorption of a water cluster around Pt surface, which excludes Nafion. This phenomenon was also observed previously for Pt nanoparticles embedded in a "bulk" Nafion membrane, where the water density increased near the Pt surface [71]. Therefore, the most hydrated system has the least Nafion coverage on the Pt nanoparticle. Since Nafion is the major contributor to the increased

adhesion in the system, it is understandable that when the Nafion–Pt interaction becomes weaker, the adhesion force becomes weaker. While this explanation has taken care of the question of why the more hydrated systems ($\lambda = 6$, 9 and 15) exhibit a weakened adhesion relative to $\lambda = 3$, it cannot explain the phenomena that the most hydrated system ($\lambda = 15$) has a slightly stronger adhesion when compared with the $\lambda = 9$ system.

Fig. 12 provides a reasonable answer to this question, namely that the adhesion between Pt and graphite is not only related to the interaction between Pt and Nafion, it is also related to the adhesion between Nafion and the graphite surface. In Fig. 12(a)–(d), a snapshot at a large separation (30 nm) is shown for the 2 nm cubic nanoparticle at $\lambda = 3$, 6, 9 and 15 respectively. At $\lambda = 3$, all of the Nafion stays on the graphite surface. At $\lambda = 6$, some of the Nafion remains on the graphite surface but some is attached to the Pt nanoparticle. At $\lambda = 9$ and 15, most of the Nafion has detached from the graphite surface. That is the detachment of the Pt nanoparticle has led to the delamination of the Nafion film from the graphite surface. It just so happens in the individual realizations given here that only partial delamination occurs at $\lambda = 15$, allowing for bridges of polymer to remain, which serve to strengthen the adhesion force. No such bridges remain at this large separation in the simulations at $\lambda = 6$ and 9.

3.2.2. Effect of Pt nanoparticle shape on Pt adhesion

In this section, we investigate the effect of nanoparticle shape at two hydration levels, $\lambda = 3$ and $\lambda = 15$. It is true that different nanoparticle shapes expose different faces of the Pt crystal. It is likely that the guiding principle in terms of nanoparticle shape should be the choice of face that yields the highest electrochemical activity. Nevertheless, it remains important for nanoparticles of any shape to adhere to the surface.

In Fig. 13, the adhesion force for four nanoparticle shapes is presented at $\lambda = 3$. For comparison purposes, the adhesion curves from the bare system are also included. From Fig. 13, it is observed
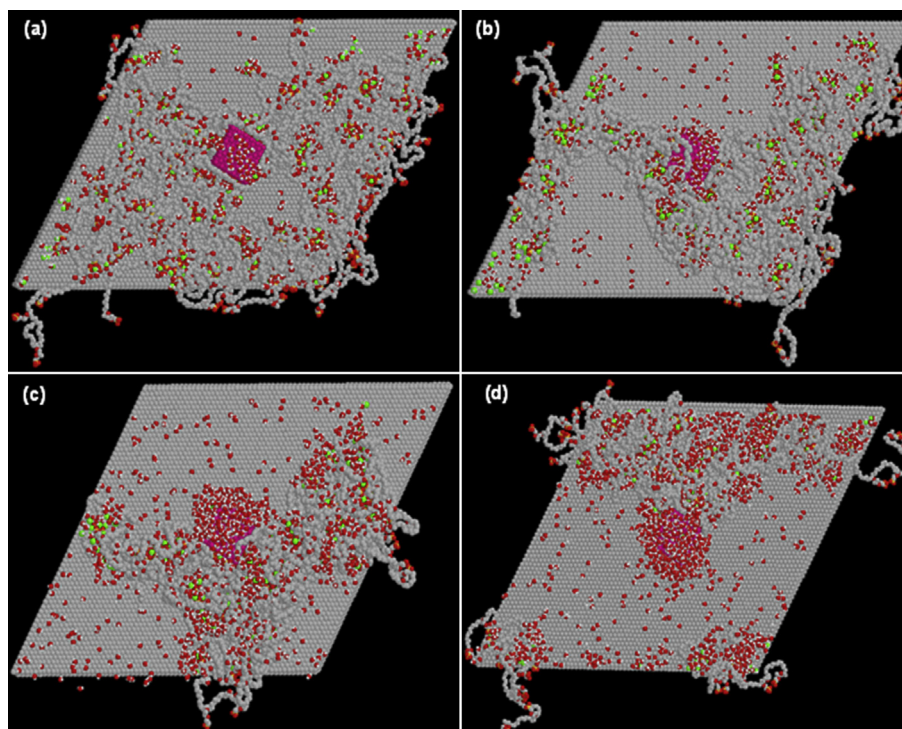

Fig. 11. Equilibrated systems contain a 2 nm cubic Pt and different hydration levels at equilibrium distance (0.32 nm). (a) $\lambda = 3$ (b) $\lambda = 6$ (c) $\lambda = 9$ (d) $\lambda = 15$.
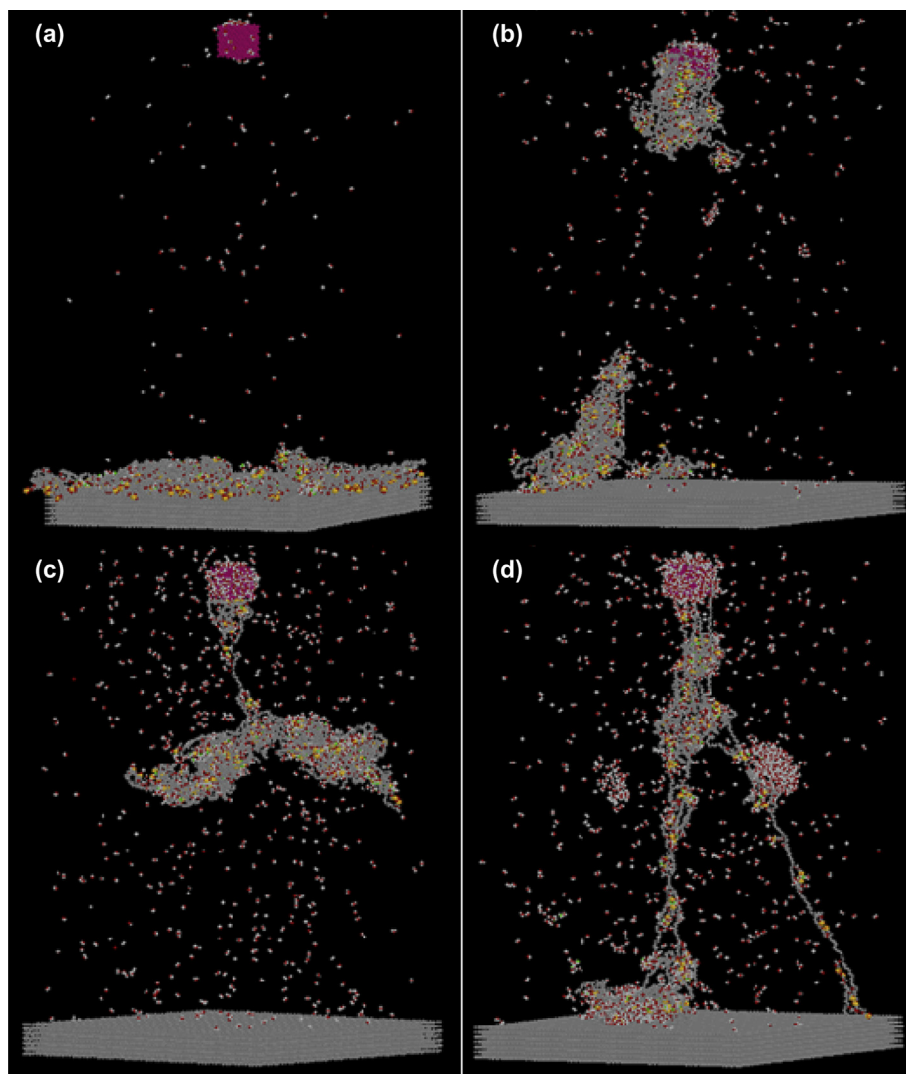
Fig. 12. Snapshots of systems contain a 2 nm cubic Pt and different hydration levels at separation distance = 30 nm. (a) $\lambda = 3$ (b) $\lambda = 6$ (c) $\lambda = 9$ (d) $\lambda = 15$.

that the maximum adhesion is enhanced with the introduction of the wet film for all particle shapes. While all the other shapes are able to reach equilibrium at around the same position in the bare and wet systems, the tetrahedral Pt has shifted its equilibrium distance from 0.32 nm to 0.39 nm (see Table 6). After examining a snapshot for the tetrahedron at 3.9 nm, it is noticed that a layer of Nafion has slipped between the Pt nanoparticle and the graphite surface, which is the cause of the equilibrium distance shift.

It is also interesting to observe the effect of nanoparticle shape on the ability to form polymer bridges, since it is at least partially through these bridges that the film fulfills its role as a binder. We intuitively expect the nanoparticle shapes with more Pt atoms to more strongly adhere to the polymer and encourage the formation and retention of bridges. In Fig. S.1(a)–(d) (Supplementary Information), snapshots of the systems with the nanoparticle (cube, tetrahedron, truncated octahedron and octahedron respectively) at a separation distance of 7.5 nm are shown. In Fig. S.2(a)–(d) (Supplementary Information), snapshots of the systems with the nanoparticle (cube, tetrahedron, truncated octahedron and octahedron respectively) at a separation distance of 12.0 nm are shown. From Fig. S.1, we can see that polymer bridges have formed in systems with three shapes of nanoparticles, all but the octahedron. In Fig. S.2, we observe that the polymer bridge has disappeared
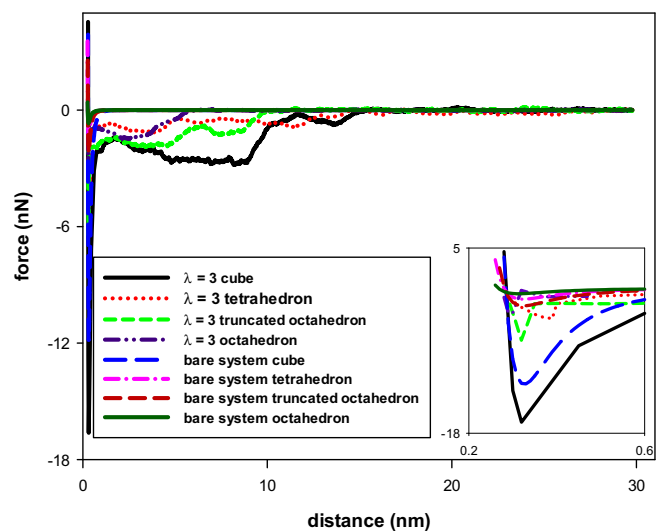

Fig. 13. Force curves for systems contain a 2 nm cubic Pt and different shapes at hydration level of $\lambda = 3$.

Table 6
Comparison of equilibrium distance and adhesion force for 2 nm Pt nanoparticle of different shapes at hydration level of $\lambda = 3$.

Pt shape	Bare system equilibrium distance	$\lambda = 3$ system equilibrium distance	Bare system adhesion force	$\lambda = 3$ system adhesion force	Adhesion force gain per atom basis
Cube	0.33 nm	0.32 nm	−11.88 nN	−16.62 nN	0.007 nN
Tetrahedron	0.32 nm	0.39 nm	−1.37 nN	−3.79 nN	0.043 nN
Truncated octahedron	0.32 nm	0.32 nm	−2.19 nN	−6.44 nN	0.014 nN
Octahedron	0.31 nm	0.30 nm	−0.68 nN	−3.09 nN	0.030 nN

from the truncated octahedron at a separation of 12 nm. Thus we partially observe our expected trend. The particles with the most Pt atoms, the cube (Fig. S.1(a)) and the truncated octahedron (Fig. S.1(c)), maintain bridges at 7.5 nm and the particle with the most Pt atoms, the cube (Fig. S.2(a)), maintains polymer bridges at 12 nm. However, contrary to the simple rule that polymer binding to the Pt nanoparticle should be a function of number of Pt atoms in the nanoparticle; it is observed that the nanoparticle with the fewest Pt atoms, the tetrahedron, also maintains bridges through 12 nm. Apparently there is something to the tetrahedral shape that allows stronger adhesion to the polymer.

Fig. S.3 (Supplementary Information) provides a close-up of the cubic and tetrahedral Pt nanoparticles at a separation of 12 nm, in order to better observe the polymer conformation on the Pt surface. As shown in Fig. S.3(a), the interaction between the cubic nanoparticle and Nafion is achieved through a tiny part of Nafion chain (mostly carbon) at the bottom of the cube (the majority of the polymer that were on the surface at distance of 7.5 nm have detached from the catalyst as the distance increased). In Fig. S.3(b), the interaction between the tetrahedral nanoparticle and Nafion is achieved through several sulfonic acid groups attached both on the bottom and side of catalyst surface, interacting with water and hydronium ions. Obviously, the interaction involves both Coulombic attraction (interaction between hydronium ion and sulfonic acid groups) and LJ attraction will be stronger than LJ attraction alone. Thus the hydrated tetrahedral system has a long-range effect due to its unique 'anchor-like' structure, i.e., its base area is much larger compared to the upper point, which allows the Pt particles to act like an anchor and more securely bind polymers during the detachment process.

Having observed the impact of nanoparticle shape on nanoparticle adhesion at a relatively low nominal water content of $\lambda = 3$,

we now turn our attention to a higher water content of $\lambda = 15$ in order to determine if the observations are independent of water content. Fig. 14 shows the filtered force results for the wettest systems ($\lambda = 15$) studied here. Most of the results are consistent with the finding obtained at the low hydration level ($\lambda = 3$). For example, the adhesion is enhanced by the introduction of the hydrated polymer film into the system, relative to the bare system. Moreover, was seen with nanoparticle size, as the hydration level goes up, more polymer will be brought away during detachment, which results in more fluctuations in the binding energy and adhesion force as a function of separation. However, we do not observe anomalous behavior of for the tetrahedral nanoparticle as was observed at the lower water content.

In Fig. S.4(a) and (b) (Supplementary Information) top and side views of a snapshot for the 2 nm tetrahedral nanoparticle at $\lambda = 15$ are shown before the detachment process starts (after the system is fully equilibrated). As was the case for the cubic nanoparticle in Fig. 11, at high water contents the tetrahedral nanoparticle is surrounded by water and is isolated from Nafion. Thus, it is not surprising that we do not see the bridging effect between Nafion/Pt and Nafion/graphite. In fact, as shown in Fig. S.4(c) (Supplementary Information), there is no polymer bridging with the tetrahedral particle at high water contents even at the very small separation distance of 1.5 nm. Without this polymer bridging, the tetrahedral particle detaches relatively easily from the surface.

3.2.3. Effect of Pt nanoparticle size on Pt adhesion

In this section, we investigate the effect of nanoparticle shape at two hydration levels, $\lambda = 3$ and $\lambda = 15$. It is true that different nanoparticle size changes the ratio of catalyst surface area to catalyst volume and thus impacts the amount of catalyst that must be present in the system. Again, it is likely that the guiding principle in terms of nanoparticle size should be optimizing electrochemical activity. However, in this section, we show that adhesion is a function of nanoparticle size and thus may be considered as a factor in selecting catalyst nanoparticle sizes for optimal performance.

Figs. S5 and S6 (Supplementary Information) show the size effect of Pt nanoparticle on adhesion force at two different water contents, $\lambda = 3$ and $\lambda = 15$. We noticed that for both hydration levels, the adhesion is a function of Pt size. As the nanoparticle size goes up, the adhesion force gets stronger, at both hydration levels. At $\lambda = 3$, the adhesion force is increased in magnitude by a factor of 1.40, 1.24, and 1.14 for the 2 nm, 4 nm and 6 nm nanoparticles respectively. At $\lambda = 15$, the adhesion force is increased in magnitude by a factor of 1.40, 1.43, and 1.31 for the 2 nm, 4 nm and 6 nm nanoparticles respectively.

4. Conclusion

The purpose of this work is to study the Pt-nanoparticle detachment mechanism from the nano-adhesion point of view. Molecular dynamics simulations were performed on various systems containing Pt nanoparticles of different sizes, shapes and Nafion thin film at four hydration levels of $\lambda = 3, 6, 9$ and 15 to investigate how the catalyst size, shape and its surrounding
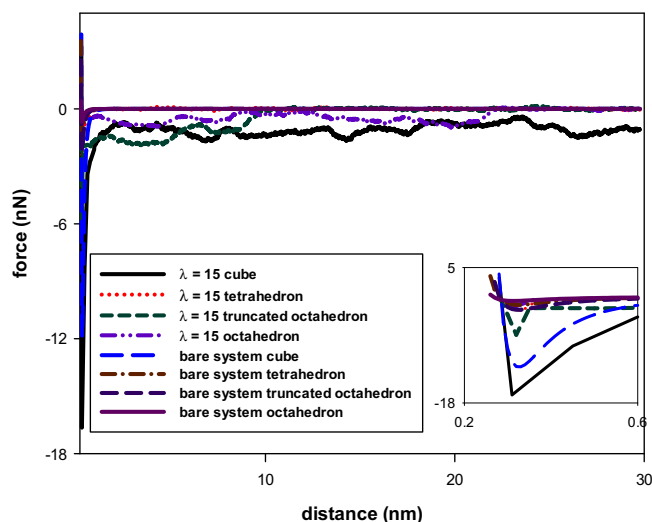

Fig. 14. Force curves for systems contain a 2 nm cubic Pt and different shapes at the hydration level $\lambda = 15$.

environment will affect adhesion. We found that bigger nano-particles yield better adhesion regardless of the humidity level. The shape of the nanoparticle can have a significant impact on adhesion. Specifically, the tetrahedron was more strongly anchored on a per atoms basis. No significant effect on the nanoparticle adhesion was observed for all the other shapes (cube, octahedron and truncated octahedron). The slight difference in adhesion force for these three shapes were due to the atom quantity difference in each shape.

The Nafion film acts like a binder to keep Pt nanoparticles in place. The hydrophobic backbone interacts with the carbon support and the hydrophilic side chain interacts well with the Pt surface as well as the water molecules and hydronium ions that are attached on it. The hydration level has a rather complicated effect on adhesion: at low hydration levels, due to the fact that water molecules will accumulate in the vicinity of the Pt nanoparticle, Nafion polymer will be excluded causing a reduction of polymer–Pt interaction, and as a result the adhesion force will decrease as the hydration level goes up. Furthermore, the extent of the decrease will be affected by the interaction between graphite surface and Nafion. When the humidity level increases beyond a certain point, polymer delamination occurs, the extent of delamination can influence the strength of interaction between Nafion and graphite. Nafion chains are more flexible at high humidity levels and there is a better chance for the hydrophobic backbone to transform to a more favorable configuration on the graphite surface, thus only partial delamination may occur. Partial delamination allows polymer chains to form bridges between graphite surface and Pt nanoparticle, which can enhance the adhesion force. In summary, the adhesion between the Pt catalyst and its support can be strengthened by controlling the nanoparticle size and shape as well as controlling the Nafion content and its humidity level in catalyst layer. This provides additional information for understanding Pt agglomeration and improving the durability of fuel cells.

Acknowledgments

Appendix A. Supplementary data

Supplementary data related to this article can be found online at http://dx.doi.org/10.1016/j.jpowsour.2013.05.011.

Nomenclature

U	potential energy
F_z	force in the z-direction
N_{Pt}	total number of atoms in the Pt nanoparticle
N_{SUR}	total number of atoms in the graphite surface
N_{FILM}	total number of atoms in the hydrated Nafion film
ε_{ij}	the depth of the LJ energy well between atoms of types i and j
σ_{ij}	the LJ collision diameter between atoms of types i and j
r_{ij}	separation between atoms of types i and j
k	Boltzmann's constant
λ	number of water molecules per sulfonic acid group

References

[1] Y. Yu, H. Li, H.J. Wang, X.Z. Yuan, G.J. Wang, M. Pan, Journal of Power Sources 205 (2012) 10–23.
[2] W. Bi, T.F. Fuller, Journal of Power Sources 178 (2008) 188–196.
[3] J. Xie, D.L. Wood, D.M. Wayne, T.A. Zawodzinski, P. Atanassov, R.L. Borup, Journal of the Electrochemical Society 152 (2005) A104–A113.
[4] S.D. Knights, K.M. Colbow, J. St-Pierre, D.P. Wilkinson, Journal of Power Sources 127 (2004) 127–134.
[5] A. Taniguchi, T. Akita, K. Yasuda, Y. Miyazaki, Journal of Power Sources 130 (2004) 42–49.
[6] D.A. Stevens, J.R. Dahn, Carbon 43 (2005) 179–188.
[7] Y. Wang, K.S. Chen, J. Mishler, S.C. Cho, X.C. Adroher, Applied Energy 88 (2011) 981–1007.
[8] G. Diloyan, M. Sobel, K. Das, P. Hutapea, Journal of Power Sources 214 (2012) 59–67.
[9] P.J. Ferreira, G.J. La O, Y. Shao-Horn, D. Morgan, R. Makharia, S. Kocha, H.A. Gasteiger, Journal of the Electrochemical Society 152 (2005) A2256–A2271.
[10] J. Aragane, T. Murahashi, T. Odaka, Journal of the Electrochemical Society 135 (1988) 844–850.
[11] K.F. Blurton, H.R. Kunz, D.R. Rutt, Electrochimica Acta 23 (1978) 183–190.
[12] G.A. Gruver, R.F. Pascoe, H.R. Kunz, Journal of the Electrochemical Society 127 (1980) 1219–1224.
[13] A. Honji, T. Mori, K. Tamura, Y. Hishinuma, Journal of the Electrochemical Society 135 (1988) 355–359.
[14] J.A.S. Bett, K. Kinoshita, P. Stonehart, Journal of Catalysis 41 (1976) 124–133.
[15] K.J.J. Mayrhofer, J.C. Meier, S.J. Ashton, G.K.H. Wiberg, F. Kraus, M. Hanzlik, M. Arenz, Electrochemistry Communications 10 (2008) 1144–1147.
[16] S. Ban, K. Malek, C. Huang, Journal of Power Sources 221 (2013) 21–27.
[17] K.L. More, K.S. Reeves, in: 2005 DOE Hydrogen Program Review (2005). Arlington, VA.
[18] M.N. Groves, C. Malardier-Jugroot, M. Jugroot, Journal of Physical Chemistry C 116 (2012) 10548–10556.
[19] Y.Y. Shao, G.P. Yin, Y.Z. Gao, Journal of Power Sources 171 (2007) 558–566.
[20] X.W. Yu, S.Y. Ye, Journal of Power Sources 172 (2007) 145–154.
[21] Y.G. Chen, J.J. Wang, H. Liu, R.Y. Li, X.L. Sun, S.Y. Ye, S. Knights, Electrochemistry Communications 11 (2009) 2071–2076.
[22] M.S. Saha, R.Y. Li, X.L. Sun, S.Y. Ye, Electrochemistry Communications 11 (2009) 438–441.
[23] T. Maiyalagan, B. Viswanathan, U. Varadaraju, Electrochemistry Communications 7 (2005) 905–912.
[24] G. Wu, D.Y. Li, C.S. Dai, D.L. Wang, N. Li, Langmuir 24 (2008) 3566–3575.
[25] X. Lepro, E. Terres, Y. Vega-Cantu, F.J. Rodriguez-Macias, H. Muramatsu, Y.A. Kim, T. Hayahsi, M. Endo, T.R. Miguel, M. Terrones, Chemical Physics Letters 463 (2008) 124–129.
[26] R.I. Jafri, N. Rajalakshmi, S. Ramaprabhu, Journal of Materials Chemistry 20 (2010) 7114–7117.
[27] S.S. Zhang, X.Z. Yuan, J.N.C. Hin, H.J. Wang, K.A. Friedrich, M. Schulze, Journal of Power Sources 194 (2009) 588–600.
[28] K. Sasaki, M. Shao, R. Adzic, Polymer Electrolyte Fuel Cell Durability, Spinger Science+Business Media, LLC, Berlin, Germany, 2009.
[29] F.A. de Bruijn, V.A.T. Dam, G.J.M. Janssen, Fuel Cells 8 (2008) 3–22.
[30] K.L. More, R.L. Borup, K.S. Reeves, ECS Transactions 3 (2006) 717–733.
[31] Z. Peng, H. Yang, Nano Today 4 (2009) 143–164.
[32] J. Chen, B. Lim, E.P. Lee, Y. Xia, Nano Today 4 (2009) 81–95.
[33] P.-C. Lee, T.-H. Han, D.O. Kim, J.-H. Lee, S.-J. Kang, C.-H. Chung, Y. Lee, S.M. Cho, H.-G. Choi, T. Kim, E. Lee, J.-D. Nam, Journal of Membrane Science 322 (2008) 441–445.
[34] X.Y. Fu, Y.A. Wang, N.Z. Wu, L.L. Gui, Y.Q. Tang, Langmuir 18 (2002) 4619–4624.
[35] M. Subhramannia, V.K. Pillai, Journal of Materials Chemistry 18 (2008) 5858–5870.
[36] E.M. Calvo-Munoz, M.E. Selvan, R. Xiong, M. Ojha, D.J. Keffer, D.M. Nicholson, T. Egami, Physical Review E 83 (2011).
[37] W.H. Qi, B.Y. Huang, M.P. Wang, Z.M. Yin, J. Li, Journal of Nanoparticle Research 11 (2009) 575–580.
[38] J.S. Yu, Reviews on Advanced Materials Science 10 (2005) 347–352.
[39] F. Coloma, A. Sepulvedaescribano, J.L.G. Fierro, F. Rodriguezreinoso, Langmuir 10 (1994) 750–755.
[40] F. Coloma, A. Sepulvedaescribano, F. Rodriguezreinoso, Journal of Catalysis 154 (1995) 299–305.
[41] J. Lee, J. Kim, T. Hyeon, Advanced Materials 18 (2006) 2073–2094.
[42] R. Andrews, D. Jacques, D.L. Qian, T. Rantell, Accounts of Chemical Research 35 (2002) 1008–1017.
[43] H.J. Dai, Accounts of Chemical Research 35 (2002) 1035–1044.
[44] K.P. De Jong, J.W. Geus, Catalysis Reviews Science and Engineering 42 (2000) 481–510.
[45] A.L. Dicks, Journal of Power Sources 156 (2006) 128–141.
[46] P. Serp, M. Corrias, P. Kalck, Applied Catalysis A General 253 (2003) 337–358.
[47] K. Lee, J.J. Zhang, H.J. Wang, D.P. Wilkinson, Journal of Applied Electrochemistry 36 (2006) 507–522.
[48] J.W. Anthony, R.A. Bideaux, K.W. BLadh, M.C. Nichols, Mineral Data Publishing, Tucson, Arizona, 2003.

[49] D.J. Keffer, https://trace.lib.utk.edu/home/davidkeffer/sites/atoms/animmn.html.
[50] J. Liu, N. Suraweera, D.J. Keffer, S. Cui, S.J. Paddison, Journal of Physical Chemistry C 114 (2010) 11279–11292.
[51] M.E. Selvan, D.J. Keffer, S.T. Cui, Journal of Physical Chemistry C 115 (2011) 18835–18846.
[52] G. Sasikumar, J.W. Ihm, H. Ryu, Journal of Power Sources 132 (2004) 11–17.
[53] H.C. Li, C. McCabe, S.T. Cui, P.T. Cummings, H.D. Cochran, Molecular Physics 101 (2003) 2157–2169.
[54] S.T. Cui, J.I. Siepmann, H.D. Cochran, P.T. Cummings, Fluid Phase Equilibria 146 (1998) 51–61.
[55] A. Vishnyakov, A.V. Neimark, Journal of Physical Chemistry B 105 (2001) 9586–9594.
[56] A. Vishnyakov, A.V. Neimark, Journal of Physical Chemistry B 105 (2001) 7830–7834.
[57] S. Cui, J. Liu, M.E. Selvan, D.J. Keffer, B.J. Edwards, W.V. Steele, Journal of Physical Chemistry B 111 (2007) 2208–2218.
[58] E. Neria, S. Fischer, M. Karplus, Journal of Chemical Physics 105 (1996) 1902–1921.
[59] W.L. Jorgensen, J. Chandrasekhar, J.D. Madura, R.W. Impey, M.L. Klein, Journal of Chemical Physics 79 (1983) 926–935.
[60] S. Urata, J. Irisawa, A. Takada, W. Shinoda, S. Tsuzuki, M. Mikami, Journal of Physical Chemistry B 109 (2005) 4269–4278.
[61] J.M.Y. Carrillo, A.V. Dobrynin, Journal of Chemical Physics 137 (2012).
[62] K.L. Johnson, K. Kendall, A.D. Roberts, Proceedings of Royal Society of London Series A Mathematical, Physical and Engineering Sciences 324 (1971) 314.
[63] B.V. Derjaguin, V.M. Muller, Y.P. Toporov, Progress in Surface Science 45 (1994) 131–143.
[64] A. Ptak, M. Kappl, S. Moreno-Flores, H. Gojzewski, H.J. Butt, Langmuir 25 (2009) 256–261.
[65] K.Q. Fan, J.Y. Jia, Y.M. Zhu, X.Y. Zhang, Chinese Physics B 20 (2011).
[66] J.Q. Feng, Colloids and Surfaces A Physicochemical and Engineering Aspects 172 (2000) 175–198.
[67] P. Attard, J.L. Parker, Physical Review A 46 (1992) 7959–7971.
[68] S.Y. Liem, K.Y. Chan, Surface Science 328 (1995) 119–128.
[69] G.W. Wu, K.Y. Chan, Journal of Electroanalytical Chemistry 450 (1998) 225–231.
[70] E.J. Lamas, P.B. Albuena, Electrochimica Acta 51 (2006) 5904–5911.
[71] M.E. Selvan, Q. He, E.M. Calvo-Munoz, D.J. Keffer, Journal of Physical Chemistry C 116 (2012) 12890–12899.
[72] D. Wolf, P. Keblinski, S.R. Phillpot, J. Eggebrecht, Journal of Chemical Physics 110 (1999) 8254–8282.
[73] S. Nose, Molecular Physics 52 (1984) 255–268.
[74] S. Nose, Journal of Chemical Physics 81 (1984) 511–519.
[75] M. Tuckerman, B.J. Berne, G.J. Martyna, Journal of Chemical Physics 97 (1992) 1990–2001.
[76] M. Kouji, S. Naruo, I. Makoto, Carbon Nanotubes – From Research to Applications, InTech, 2011.
[77] N.W. Khun, E. Liu, Surface & Coatings Technology 205 (2010) 853–860.
[78] X.L. Zhang, X.H. Zhong, X. Meng, G.W. Yi, J.H. Jia, Tribology Letters 46 (2012) 65–73.
[79] M.E. Selvan, J. Liu, D.J. Keffer, S. Cui, B.J. Edwards, W.V. Steele, Journal of Physical Chemistry C 112 (2008) 1975–1984.
[80] J.W. Liu, M.E. Selvan, S. Cui, B.J. Edwards, D.J. Keffer, W.V. Steele, Journal of Physical Chemistry C 112 (2008) 1985–1993.
[81] M.J. Park, K.H. Downing, A. Jackson, E.D. Gomez, A.M. Minor, D. Cookson, A.Z. Weber, N.P. Balsara, Nano Letters 7 (2007) 3547–3552.